Supplementary Information (SI) for Journal of Materials Chemistry A.

Supplementary information

Lattice plainification and high symmetry enhance the thermoelectric performance of n-type Bi_2Te_3-based materials

Chao Liang,[a] Yi Wen,[b] Shulin Bai,[b] Rong Liu,[a] Huiqiang Liang,[c] Xin Qian,[c] Yating Yuan,[a] Xiaoqian Wang,[a] Xiaokun Feng,[a] Zhenguo Bai,[a] Wanxuan Chen,[a] Yiqing Jia,[a] Tian Gao,[b] Sining Wang,[b] Yuting Qiu,[b] Yongjin Chen,[d] Xiang Gao,[d] Haonan Shi,*[a] Lizhong Su *[ae] and Peikang Bai *[ae]

[a] School of Materials Science and Engineering, Taiyuan University of Science and Technology, Taiyuan, 030024, China.
[b] School of Materials Science and Engineering, Beihang University, Beijing, 100191, China.
[c] College of Physics Science and Technology, Hebei University, Baoding, 071002, China.
[d] Center for High Pressure Science and Technology Advanced Research (HPSTAR), Beijing, 100094, China.
[e] Shanxi Provincial Key Laboratory for Controlled Metal Solidification and Additive Manufacturing, Taiyuan, 030051, China.
Corresponding author email: shihaonan@tyust.edu.cn; sulizhong@tyust.edu.cn; baipeikang@nuc.edu.cn

1. Experimental details

1.1 Material synthesis and processing

High-purity elements including indium (99.9999%, Beijing Innochem, China), bismuth (99.999%, Hebei Jiuyue, China), tellurium (99.999%, Hebei Jiuyue, China), and selenium (99.999%, Hebei Jiuyue, China) were used in the experiment. First, the raw elements were weighed according to stoichiometric ratios and sealed in quartz tubes, which were stored under a vacuum pressure of 10-4 Pa. Subsequently, the samples were placed in a furnace (heated from room temperature to 1373 K for 13 hours, held for 10 h, then cooled naturally to room temperature). The resulting alloy powder was ground to approximately 75 microns using an FL-01 mill for subsequent spark plasma sintering (SPS) (SPS-2T-20-mini, Nanjing Boyuntong, China). The powder was pressed into Ø12.7 mm graphite molds at 713 K and 50 MPa pressure for 5 min.

1.2 Structure characterization:

The phase composition and preferred orientation of the samples were characterized by X-ray diffraction (XRD) (FRINGE CLASS-SY X-ray, Suzhou Langsheng, China) using a X-ray diffractometer (Cu Kα radiation, λ=1.5418 Å) and operating at 30 kV and 16 mA.

X-ray photoelectron spectroscopy:

The chemical valences and compositions of $In_{0.01}Bi_2Te_{2.6}Se_{0.4}$ were analyzed using an X-ray photoelectron spectrometer (XPS) (ESCALAB 250Xi, Thermo Fisher Scientific Inc., America) with an Al Kα radiation source (1486.6 eV photon energy, 300 W) at 10^{-19} Pa pressure.

HAADF-STEM characterizations:

The $In_{0.0001}Bi_2Te_{2.6}Se_{0.4}$ bulk samples were thinned to lamellas by FIB and soldered to heating chips (Wildfire Nano-Chip, DENSsolutions, Netherlands) for in situ experiments. The HAADF-STEM images were acquired using an aberration-corrected STEM (JEM-ARM200F, JEOL, Japan) operating at an acceleration voltage of 200 kV.

Vickers hardness test:

The Vickers hardness of Bi_2Te_3, $Bi_2Te_{2.6}Se_{0.4}$ and $In_{0.0001}Bi_2Te_{2.6}Se_{0.4}$ on their cleavage plane was measured by Digital display microhardness test system (SΛΛCOO, HVS-1000Z, CHN) with a pyramidal diamond indenter having a face angle of 136°. A load of 0.1 kgf was applied to the cleavage PLANE for a dwell time of 15 seconds (HV0.1/15). The resulting pyramidal impressions were measured using an optical microscope attached to the hardness tester. For each sample, ten indentations were made at randomly selected locations to obtain a statistically reliable average value (Table. S1).

1.3 Electrical transport properties measurement:

Cylindrical samples were cut into rectangular blocks measuring 3 × 3 × 10 mm^3. Using the commercial measurement instrument CTA-3 (Cryoall, China), simultaneous measurements of electrical conductivity and Seebeck coefficient were performed in a helium atmosphere from room temperature to 523 K. The measurement uncertainty was 5%.

The Hall coefficient RH of the samples was measured using the Van der Pauw method (CH-500 High/Low Temperature Hall Effect Testing System, Beijing Cuihai Jiacheng Magnetoelectric Technology, China). The samples used were square thin slices approximately 6 mm wide and 0.5-1 mm thick. The Hall carrier concentration nH was calculated according to formula: $n_H = \frac{1}{eR_H}$, where *e* is the elementary charge.

1.4 Thermal transport properties measurements:

A 6 mm × 6 mm × 1 mm thick square prismatic sample was polished and coated with a thin layer of graphite to minimize measurement errors when determining the thermal diffusivity coefficient D using a CLA 1000 cryogenic thermal conductivity analyzer (Cryoall, China). The total thermal conductivity was calculated using the formula $\kappa_{tot} = \rho DC_p$, where C_p is the heat capacity calculated via the Debye model, and ρ is quantified based on the sample dimensions and mass. Subsequently, the lattice thermal conductivity κ_{lat} was determined by directly subtracting the electronic thermal conductivity κ_{ele} from κ_{tot}. The electronic thermal conductivity κ_{ele} is calculated using the Lorentz number L, electrical conductivity σ, and absolute temperature T via the formula $\kappa_{ele} = L\sigma T$.

1.5 Orientation degree f:

The orientation factor f, calculated using the Lotgering method, is given by the following formula to quantify the orientation degree of samples:

$$f = \left(P - P_0\right)/\left(1 - P_0\right) \tag{S1}$$

$$P_0 = I_0(00l)/\sum I_0(\mathrm{h}kl) \tag{S2}$$

$$P_0 = I(00l)/\sum I(\mathrm{h}kl) \tag{S3}$$

There, I(00l) is the integral peak intensity for the preferred samples and I_0(00l) is for the randomly oriented samples.

Biaxial X-ray diffraction tests were conducted on $Bi_2Te_{2.6}Se_{0.4}$ bulk samples, performed both perpendicular to the sintering pressure direction (⊥) and parallel to it (//), as detailed in **Fig. S3**. All diffraction patterns exhibited perfect agreement with the $Bi_2Te_{2.6}Se_{0.4}$ structure, confirming no structural transformation occurred during thermal deformation. The (00l) peak intensity was significantly higher in the perpendicular direction than in the parallel direction, indicating that the in-plane orientation of $In_{0.0001}Bi_2Te_{2.6}Se_{0.4}$ layered grains reoriented during SPS sintering to become perpendicular to the pressure direction, thereby enhancing preferred orientation.

1.6 The preparation process of thermoelectric device particles:

Cut $In_{0.0001}Bi_2Te_{2.6}Se_{0.4}$ wafers perpendicular to the pressure direction to obtain 3 mm thick wafers, then cut them into 3×3×5 mm^3 rectangular blocks.

Polish the upper and lower surfaces of the sample discs using 1000-grit, 2000-grit, and 3000-grit sandpaper.

Clean the samples using ultrasonic cleaning equipment.

Immerse the samples in an acidic solution (concentrated hydrochloric acid mixed with deionized water at a 1:1 ratio) for surface cleaning, then remove the acid solution using ultrasonic equipment.

Apply a nickel coating to both surfaces of the samples via chemical plating (plating solution model Q/YS.602-2).

Finally, $Sn_{96.5}Ag_{3.0}Cu_{0.5}$ solder was used for both the cold end and hot end, employing single-leg soldering with a reflow oven manufactured (Shandong Puhui Technology Reflow Soldering, China).

1.7 Single-leg power generation efficiency test:

We tested the $In_{0.0001}Bi_2Te_{2.6}Se_{0.4}$-based single-leg (3 mm×3 mm×10 mm) module using TE-X-MS device, with the comprehensive results presented in **Fig. 6d**. This equipment provides the temperature difference ΔT across both ends of the single-leg module and the resulting voltage ΔV. The voltage ΔV determined by the temperature difference forms the temperature difference value S. When current I is applied, the current dependence of power output P is as follows:

$$P = I(\Delta V - IR) = - RI^2 + S\Delta TI \tag{S4}$$

During the measurement process, the maximum power output P_{max} can be calculated based on the current dependence relationship. Here, the resistance R represents the internal resistance value. This instrument employs a flow meter to measure heat flux. The relationship between the temperature difference between the inlet temperature T_{in} and the outlet temperature T_{out} of the liquid in the flow meter and the liquid flow velocity v, as well as the module heat flux, is expressed by the following equation:

$$T_{out} - T_{in} = \frac{Q1}{Cv} \tag{S5}$$

In the equation, C represents the specific heat capacity per unit volume. Within the analysis software, heat flux can be calculated using the rate of change in temperature difference between the liquid inlet and outlet temperatures, along with the flow velocity. The relationship between heat flux Q and conversion efficiency η for the thermoelectric module is expressed as follows: $\eta = \frac{P}{Q + P}$.

This heat flow comprises the heat Q_0 generated by the temperature difference across the sample and the amount of Joule heat produced, expressed as:

$$Q = Q(0) + ST_C I + \frac{1}{2} I^2 R \tag{S6}$$

The sample temperature at the low-temperature end is denoted as T_{C}. The conversion efficiency is calculated using the following formula:

$$\eta = \frac{RI^2 + S(T_H - T_C)I}{-\frac{1}{2}RI^2 + ST_H I + Q(0)} \tag{S7}$$

The theoretical power generation efficiency of a single-leg thermoelectric generator is calculated as follows：

$$\eta_{\max} = \frac{T_{\mathrm{h}} - T_{\mathrm{c}}}{T_{\mathrm{h}}} \frac{\sqrt{1 + \overline{Z}\overline{T}} - 1}{\sqrt{1 + \overline{Z}\overline{T}} + T_{\mathrm{c}} / T_{\mathrm{h}}} \tag{S8}$$

2 Supplementary Figures

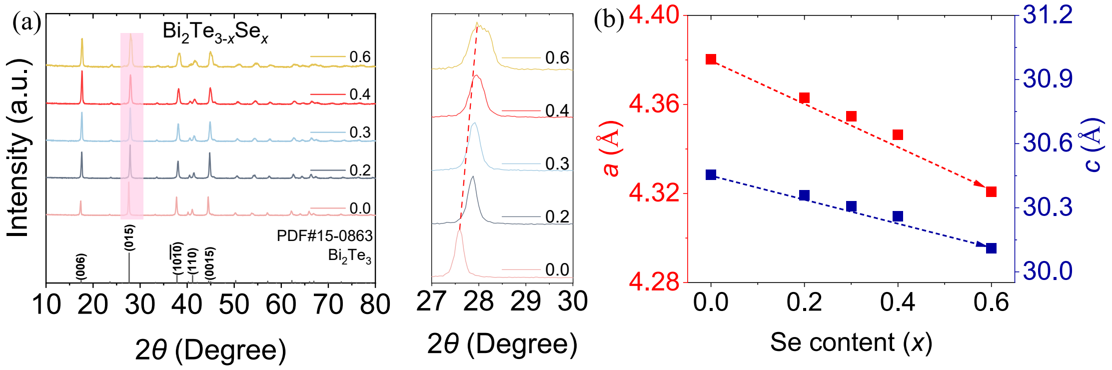

Figure S1. (a) XRD pattern and enlarged section of $Bi_2Te_{3-x}Se_x$ (b) Refined lattice constant variation curves along the a-axis and c-axis directions.

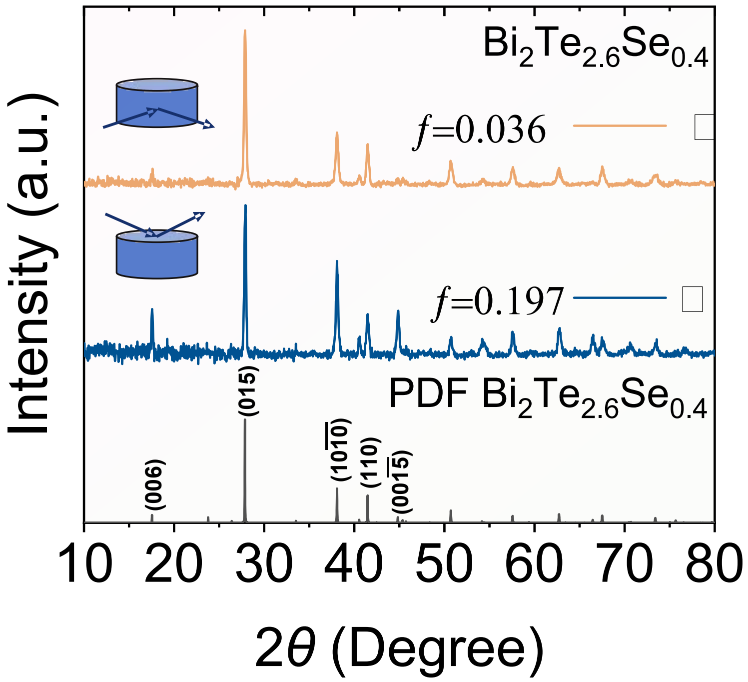

Figure S2. XRD distribution patterns of $Bi_2Te_{2.6}Se_{0.4}$ in the directions perpendicular (⊥) and parallel (//) to the SPS pressure direction.

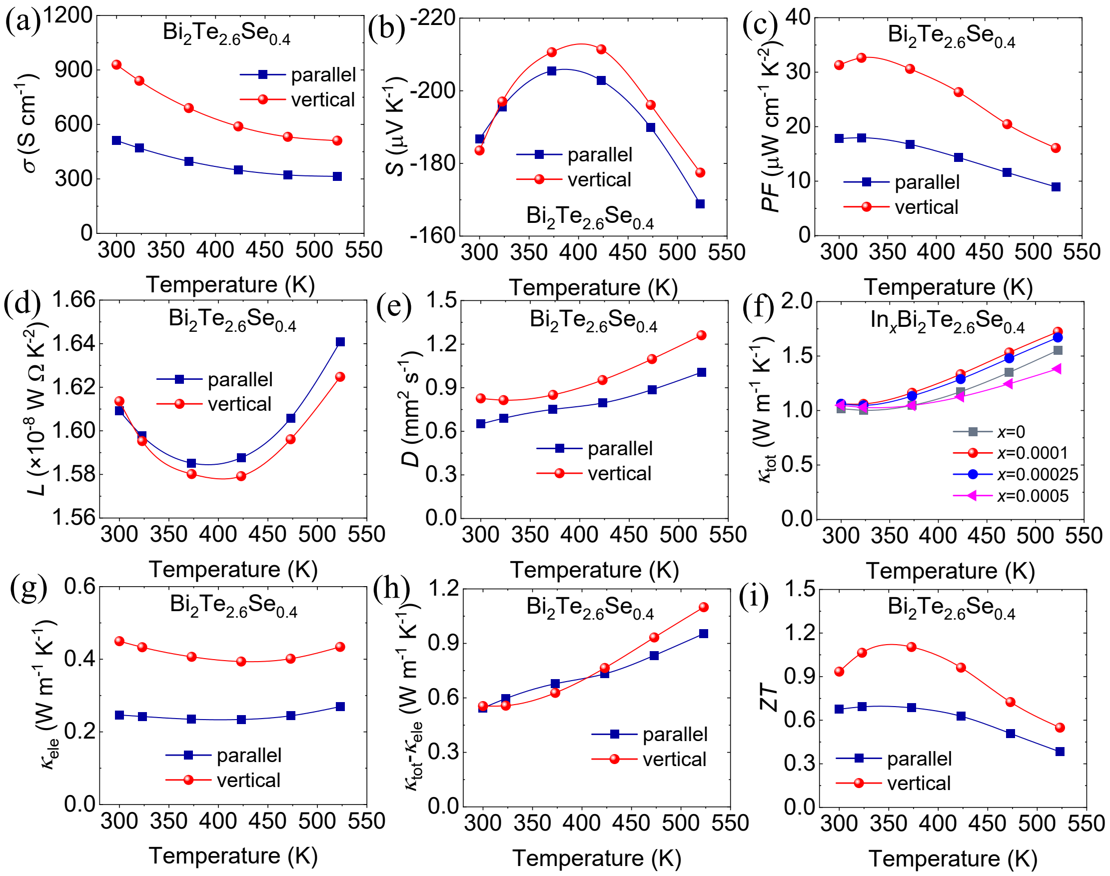

Figure S3. Electrical and thermal transport properties of $Bi_2Te_{2.6}Se_{0.4}$ perpendicular and parallel to the SPS pressure direction. (a) Seebeck coefficient. (b) Electrical conductivity. (c) Power factor. (d) Lorentzian constant. (e) Thermal diffusivity. (f) Total thermal conductivity. (g) Electronic thermal conductivity. (h) κ_{tot} - κ_{ele}. (i) *ZT*.

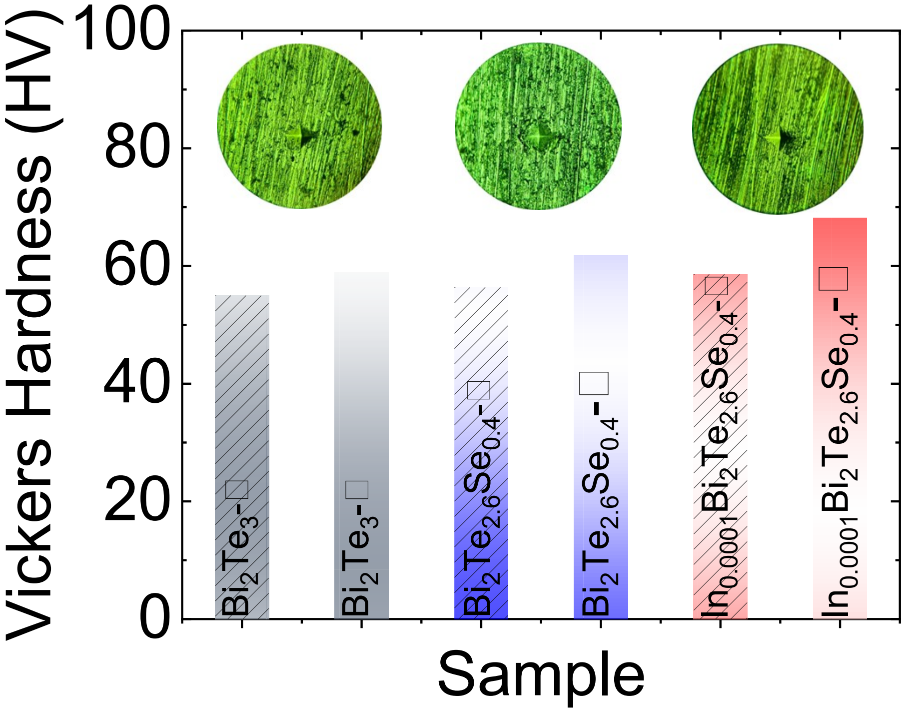

Figure S4. Vickers hardness of SPS-sintered n-type Bi_2Te_3-based polycrystalline samples.

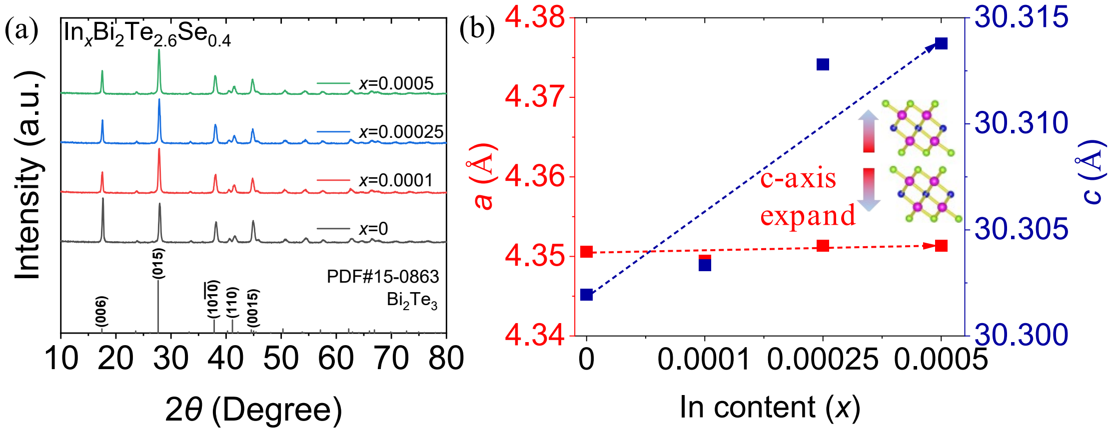

Figure S5. (a) XRD pattern of In$_x$Bi$_2$Te$_{2.6}$Se$_{0.4}$ (b) Refined lattice constant variation curves along the a-axis and c-axis directions.

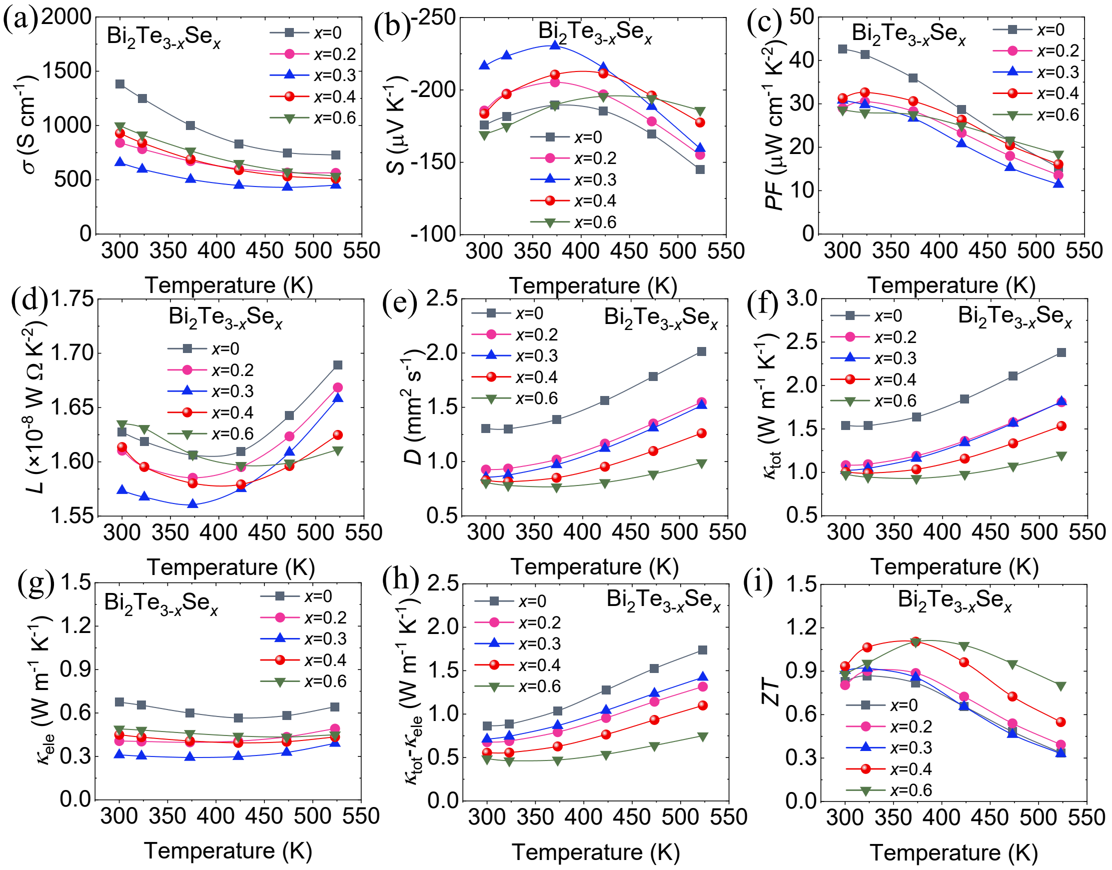

Figure S6. Electrical and thermal transport properties of Bi$_2$Te$_{3-x}$Se$_x$ (x = 0-0.6). (a) Electrical conductivity. (b) Seebeck coefficient. (c) Power factor. (d) Lorentzian constant. (e) Thermal diffusivity. (f) Total thermal conductivity. (g) Electronic thermal conductivity. (h) κ_{tot} - κ_{ele}. (i) ZT.

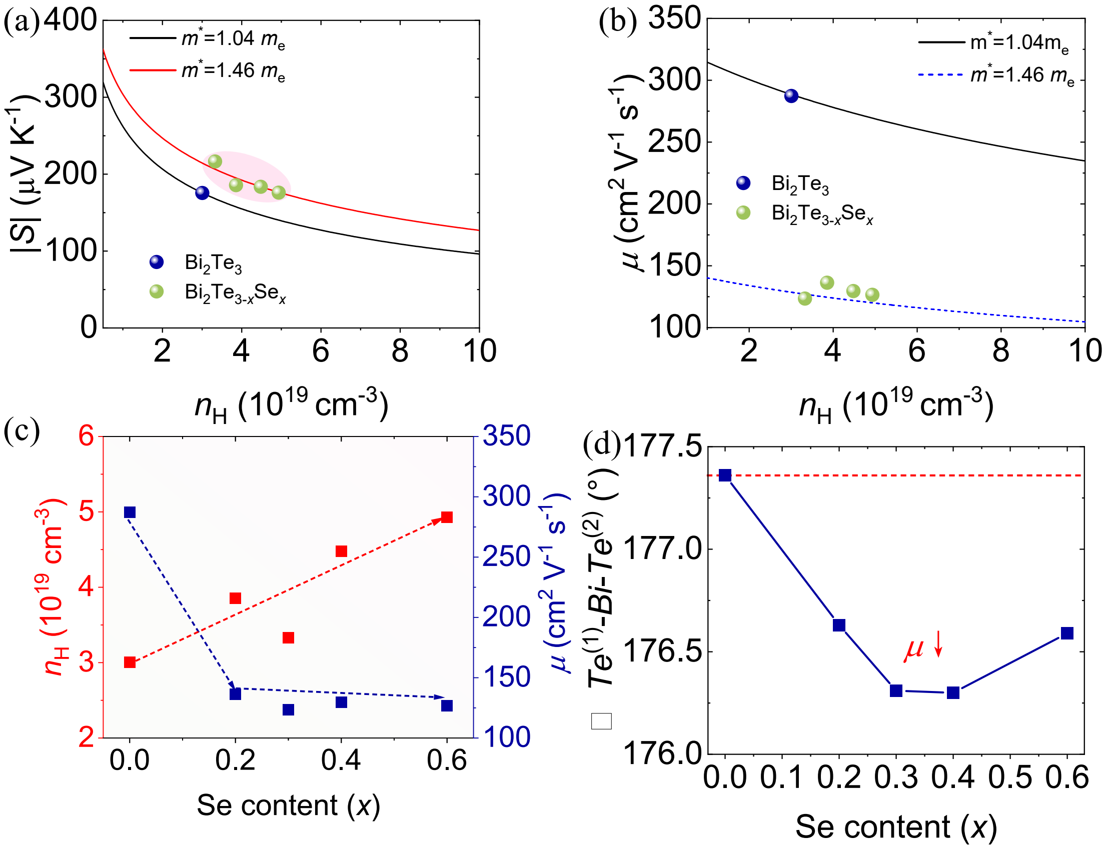

Figure S7. (a) Pisarenko plot of $Bi_2Te_{3-x}Se_x$ at x = 0-0.6 under ambient conditions. (b) Relationship between carrier concentration and room-temperature mobility. (c) Variation curves of carrier concentration and mobility. (d) Variation curve of the ∠$Te^{(1)}$-Bi-$Te^{(2)}$ bond angle with increasing Se doping concentration.

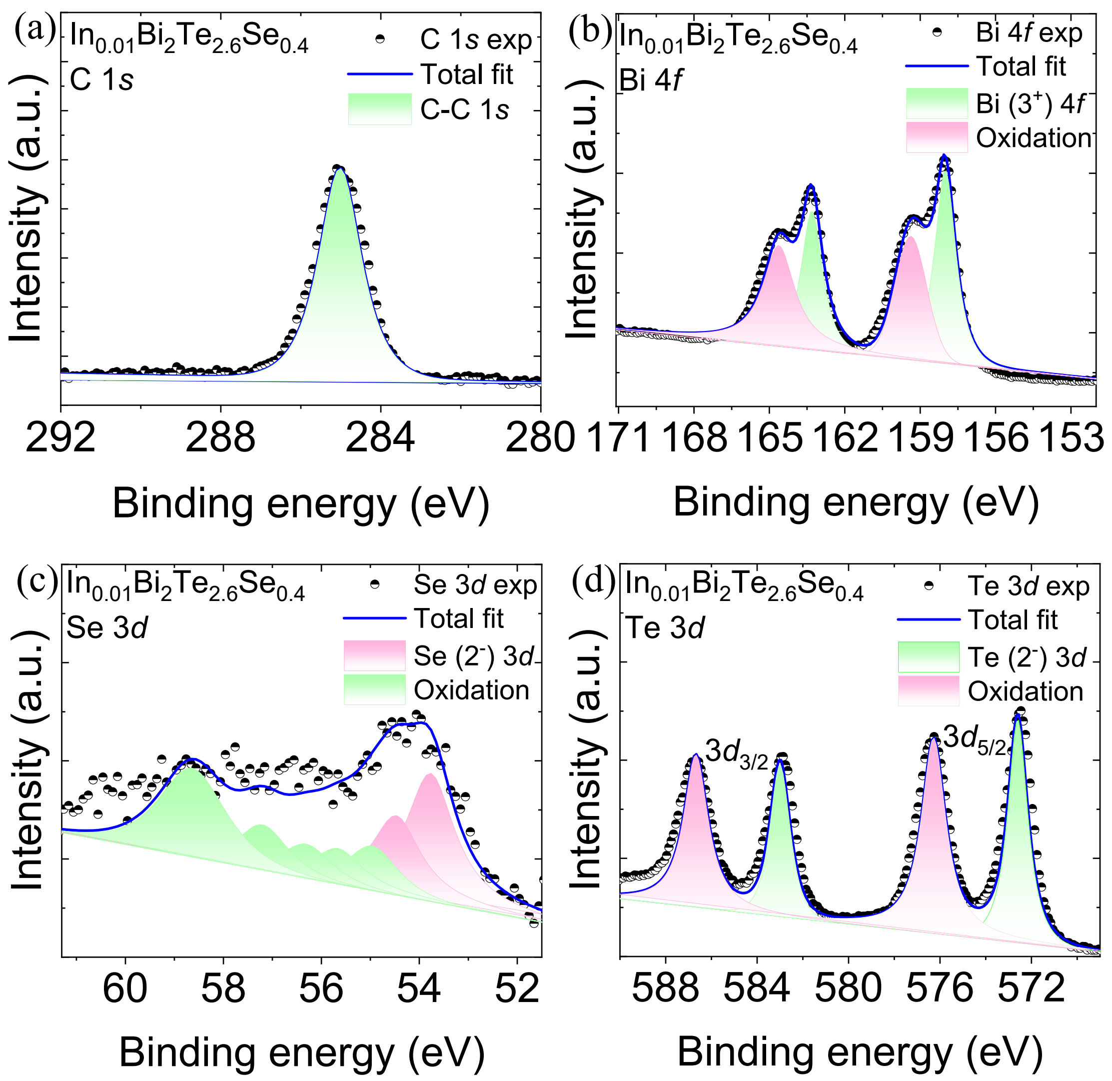

Figure S8. The X-ray photoelectron spectroscopy (XPS) of SPS-sintered $In_{0.01}Bi_2Te_{2.6}Se_{0.4}$ sample. The spectrum of (a) C. (b) Bi. (c) Se. (d) Te.

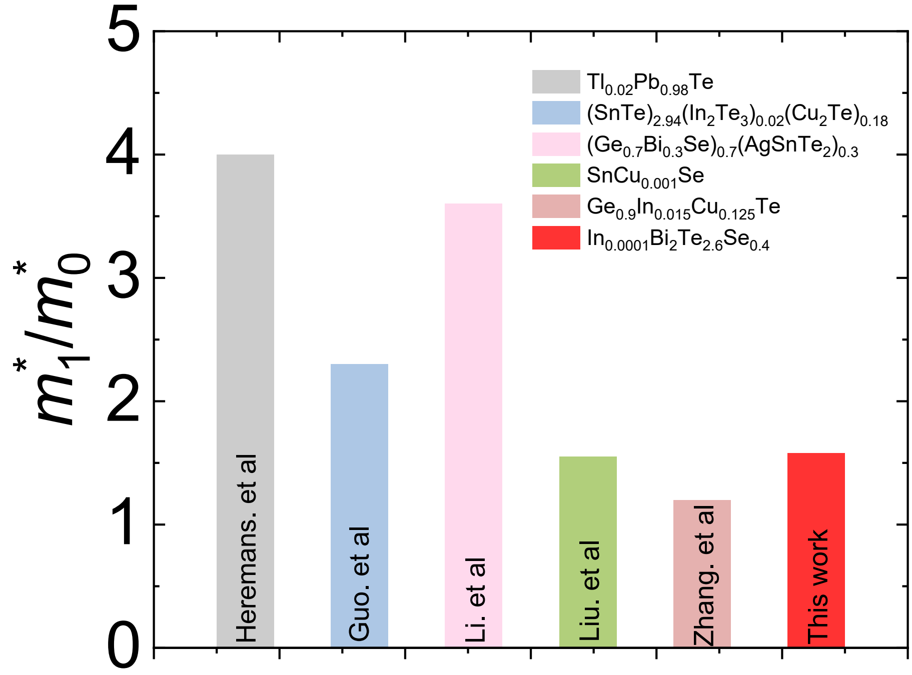

Figure S9. Quantifying the contribution of different elemental doping to band resonance in various thermoelectric materials using m^*_1/m^*_0 analysis [1-5].

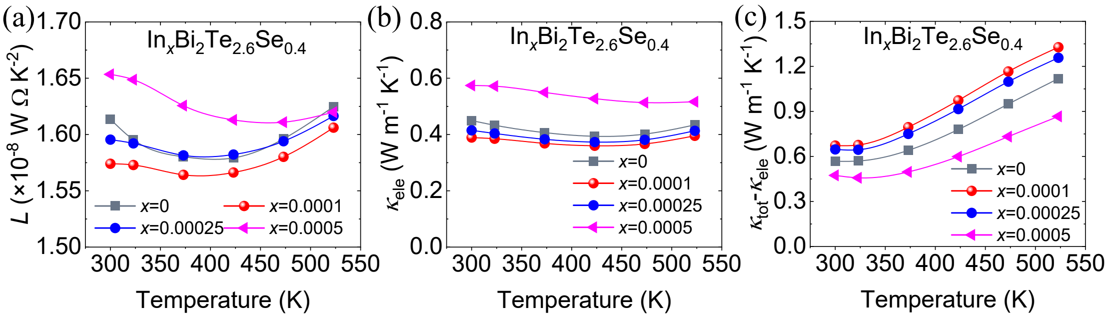

Figure S10. Electrical and thermal transport properties of $In_xBi_2Te_{2.6}Se_{0.4}$. (a) Lorentzian constant. (b) Electronic thermal conductivity. (c) κ_{tot} - κ_{ele}.

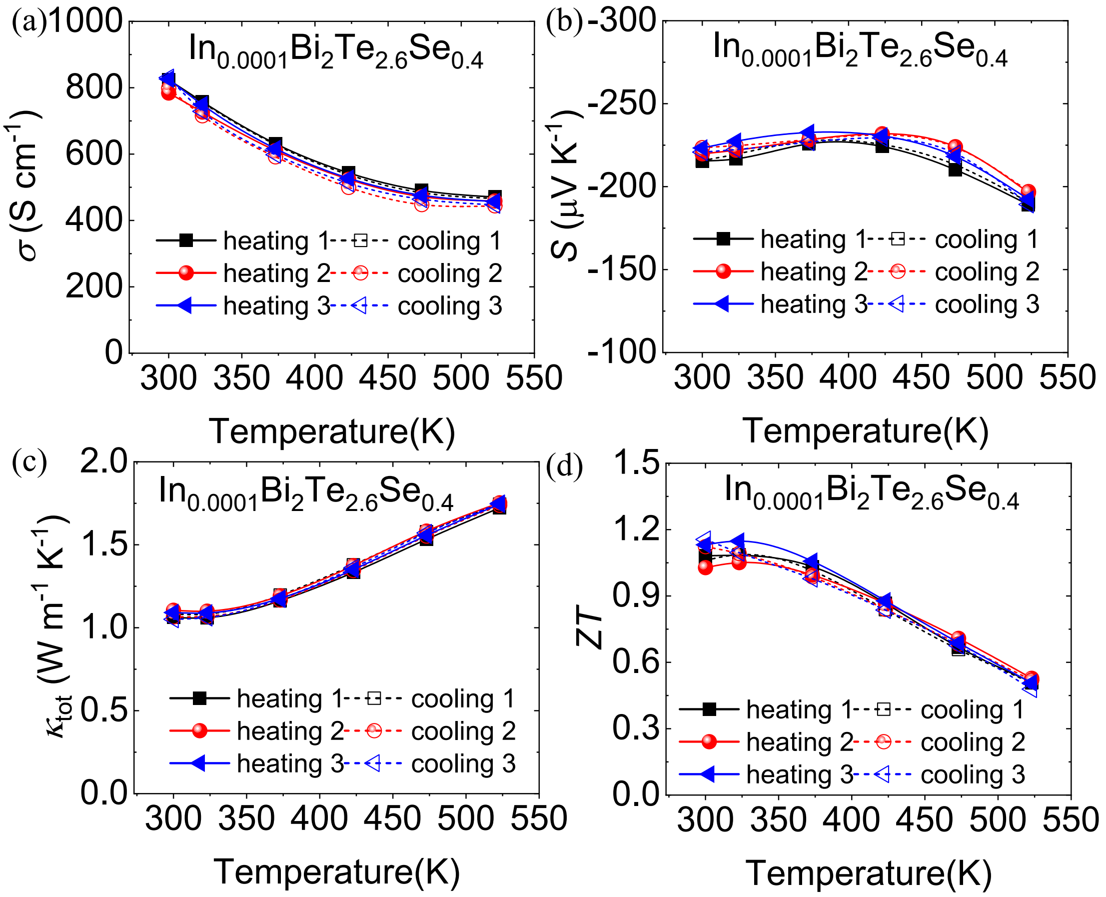

Figure S11. Cycling stability test of $In_{0.0001}Bi_2Te_{2.6}Se_{0.4}$ sample. (a) Electrical conductivity. (b) Seebeck coefficient. (c) Total thermal conductivity. (d) *ZT*.

3 Supplementary Table

Table S1. Vickers hardness of Bi_2Te_3, $Bi_2Te_{2.6}Se_{0.4}$ and $In_{0.0001}Bi_2Te_{2.6}Se_{0.4}$ parallel and vertical to the SPS plane.

Sample	Depth (mm)	D1 (μm)	D2 (μm)	HV	HV_{ave}
Bi_2Te_3(parallel)	1.00	58.087	56.371	54.6	55.0
	1.20	55.881	56.861	56.4	
	1.40	58.087	58.087	54.2	
Bi_2Te_3(vertical)	1.00	56.861	55.391	58.9	58.9
	1.20	59.557	58.822	52.9	
	1.40	53.185	53.675	65.0	
$Bi_2Te_{2.6}Se_{0.4}$(parallel)	1.00	61.763	58.822	55.1	56.4
	1.20	56.861	57.841	57.4	
	1.40	58.577	56.861	56.7	
$Bi_2Te_{2.6}Se_{0.4}$(vertical)	1.00	55.881	57.106	58.1	61.8
	1.20	52.940	53.920	65.0	
	1.40	53.185	55.881	62.4	
$In_{0.0001}Bi_2Te_{2.6}Se_{0.4}$(parallel)	1.00	54.165	52.449	65.3	58.6
	1.20	58.577	60.292	52.5	
	1.40	55.391	57.596	58.1	
$In_{0.0001}Bi_2Te_{2.6}Se_{0.4}$(vertical)	1.00	59.557	59.067	60.3	68.2
	1.20	51.224	52.695	73.7	
	1.40	53.675	50.979	70.7	

References

[1]Qingtang Zhang,Zhuoyang Ti,Yuelei Zhu, et al. Achieving Ultralow Lattice Thermal Conductivity and High Thermoelectric Performance in GeTe Alloys via Introducing Cu_2Te Nanocrystals and Resonant Level Doping[J]. Acs Nano, 2021, 15: 19345-19356.

[2]Fengkai Guo,Bo Cui,Huiyuan Geng, et al. Simultaneous Boost of Power Factor and Figure-of-Merit in In–Cu Codoped SnTe[J]. Small, 2019, 15: 1902493.

[3]Joseph P.Heremans,Vladimir Jovovic,Eric S.Toberer, et al. Enhancement of Thermoelectric Efficiency in PbTe by Distortion of the Electronic Density of States[J]. Science, 2008, 321: 554.

[4]Yu-Geng Li,Yong-Qiang Liu,Mo-Ran Wang, et al. Leveraging crystal symmetry for thermoelectric performance optimization in cubic GeSe[J]. Rare Metals, 2024, 43(10): 5332-5345.

[5]Dongrui Liu,Dongyang Wang,Tao Hong, et al. Lattice plainification advances highly effective SnSe crystalline thermoelectrics[J]. Science, 2023, 380: 841-846.